Second harmonic generation on the yellow 1*S* exciton in Cu_2O in symmetry-forbidden geometries

Johannes Mund,[1] Christoph Uihlein,[1] Dietmar Fröhlich,[1] Dmitri R. Yakovlev,[1,2] and Manfred Bayer[1,2]
[1]*Experimentelle Physik 2, Technische Universität Dortmund, D-44221 Dortmund, Germany*
[2]*Ioffe Institute, Russian Academy of Sciences, 194021 St. Petersburg, Russia*

(Received 8 April 2019; published 21 May 2019)

We observe optical second harmonic generation (SHG) on the 1*S* exciton resonance of the yellow exciton series in Cu_2O in four crystal directions ([001], $[\bar{1}10]$, $[11\bar{2}]$, and [111]). For light with the *k*-vector parallel [001] and $[\bar{1}10]$, SHG is symmetry forbidden in an ideal crystal according to band structure. We explain the observation of SHG signals in the forbidden geometries by local strain inducing splitting and mixing of the 1*S* components. Experimental data and a microscopic theory confirm that this effect observed on the 1*S* exciton requires a relatively long exciton lifetime. The SHG signals of excitons with principal quantum number $n \geqslant 2$ are compliant with selection rules derived by group theory from the symmetry of an unstrained crystal.

DOI: 10.1103/PhysRevB.99.195204

I. INTRODUCTION

Nonlinear optics has established itself as a broad field of research in modern optics [1,2]. Due to the additional degrees of freedom in spectroscopic investigations where more than one photon are participating detailed information on electronic properties of solids can be gained, which is not accessible to one-photon experiments [3]. Second harmonic generation (SHG) [4] and two-photon absorption (TPA) [5,6] were the first nonlinear methods applied in solid-state spectroscopy. In TPA experiments, wave vector and polarization of the incoming photons can be set to excite a transverse polariton as well as longitudinal exciton resonances [7]. In SHG, however, the additional polarization of the outgoing photon has to be taken into account, which limits SHG to transverse polariton resonances [8]. The application of electric and magnetic fields opens up further information on details of exciton and polariton resonances [9].

Cu_2O with its illustrative exciton series of high binding energy is well suited for studying the fundamental properties of excitons. Being the first semiconductor to show Wannier-Mott excitons [10], Cu_2O attracted continuing interest recently [11,12]. The first experiments of SHG on the 1*S* exciton in Cu_2O were reported in Ref. [13]. In a previous publication [14], we studied in detail SHG on excitons of the yellow series of Cu_2O up to $n = 9$. Despite the fact that Cu_2O has inversion symmetry, and thus, SHG is forbidden for dipole transitions, we observed SHG from even-parity *S* and *D* excitons and from odd-parity *P* excitons. This was explained by replacing one of the three dipole operators of the SHG process by a quadrupole operator. By a merely group theoretical analysis with use of the tables of Koster *et al.* [15] we derived the polarization selection rules for linearly and circularly polarized light.

We found for even *S* excitons with principal quantum number $n \geqslant 2$ only SHG for laser light *k* directions along crystal axes of lower symmetry (e.g., [111], $[11\bar{2}]$) where excitation by two dipoles and emission by one quadrupole is allowed [Fig. 1(a)]. For the 1*S* exciton, however, strong SHG signals were found for forbidden crystallographic directions (e.g., [001], $[\bar{1}10]$), too. These directions are called forbidden because two photons excite combinations of exciton components that do not allow emission by a quadrupole [Fig. 1(b)]. The goal of this paper is to clarify the discrepancy at the 1*S* exciton state.

In a previous experiment on time-resolved two-photon emission [16], a similar observation was made. After resonant quadrupole excitation of a 1*S* component, a delayed signal from an orthogonal 1*S* component was detected. These findings were explained by relaxation processes between exciton components. We want to emphasize that in this contribution for SHG we are dealing with a different situation. We coherently excite by two photons through dipole transitions a resonance on the quadrupole exciton-polariton at a smaller wave vector (due to smaller refractive index at half the photon energy) and lower energy (due to spatial dispersion) than the previous resonant excitation by a one-photon quadrupole transition. As will be outlined in detail in Sec. IV, we explain our findings by a strain-induced mixing of the 1*S* components. Strain-induced effects in Cu_2O were also reported in Refs. [17–19] using linear spectroscopy. Strain parameters were investigated experimentally in Ref. [20] and theoretically in Ref. [21].

The paper is organized as follows: In Sec. II, we briefly present the experimental technique. In Sec. III, we show rotational diagrams for SHG forbidden and allowed crystal orientations. In Sec. IV, we introduce our theoretical concept of a strain- and band-structure-induced mixing of 1*S* orthoexciton states that makes them active for SHG. By fitting we obtain appropriate strain parameters and are able to simulate in detail the observed polarization dependences of SHG signals (Sec. V). The role of the exciton lifetime and implications from the fitting procedure are discussed in Sec. VI. In Sec. VII, we summarize the results and give a short outlook.

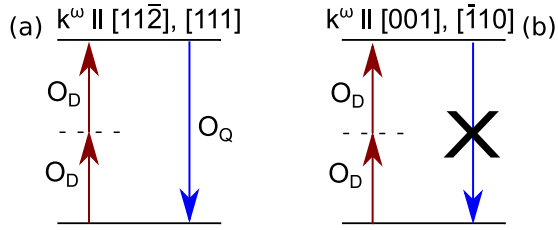

FIG. 1. Schematics of (a) SHG in allowed and (b) SHG in forbidden k directions for S-exciton states in an ideal Cu_2O crystal. O_D and O_Q denote photon transitions in dipole and quadrupole approximations, respectively.

II. EXPERIMENT

The setup is described in detail in Ref. [14]. In Fig. 2, we illustrate the configuration of the SHG experiment. Excitation of the sample is performed by laser pulses of 200-fs duration with a full width at half maximum (FWHM) of ≈10 meV. The energy per pulse was set to 0.3 μJ at a repetition rate of 30 kHz. Using an optical parametric amplifier system, the laser radiation with wave-vector $\mathbf{k}^{\omega}$ can be tuned in frequency ω. To excite the 1S exciton resonance the output photon energy is set to 1.016 or to 1.082 eV for higher-n exciton states. The laser beam is adjusted to impinge perpendicularly on the crystal surface and focused to a spot size of about 100 μm. Detection of the SHG signal with 2ω and $\mathbf{k}^{2\omega} = 2\mathbf{k}^{\omega}$ is provided by a 0.5-m monochromator (Acton, Roper Scientific) with a 1800-grooves/mm grating in combination with a silicon charge-coupled device (CCD) camera. Total spectral resolution of the system is 100 μeV. To record exciton spectra, the laser photon energy is not scanned. We use instead our recently demonstrated approach with spectrally broad femtosecond laser pulses where the resolution is determined by the spectrometer used for signal detection [14].

With a Glan-Thompson polarizer and a half-wave plate, the linear polarization of the incoming and outgoing light can be varied continuously and independently. One can thus measure for any fixed polarization of $\mathbf{E}^{\omega}$ or $\mathbf{E}^{2\omega}$ the angular dependence of the other polarization. We, however, choose to measure the rotational anisotropies of the SHG signals for either parallel ($\mathbf{E}^{\omega} \parallel \mathbf{E}^{2\omega}$) or crossed ($\mathbf{E}^{\omega} \perp \mathbf{E}^{2\omega}$) linear polarizations of the laser and the SHG.

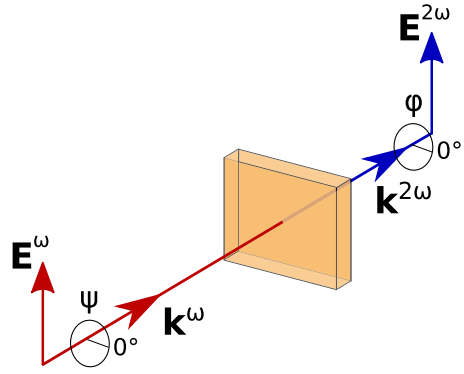

FIG. 2. Schematics of experimental configuration: Light k-vectors $\boldsymbol{k}^{\omega,2\omega}$ are perpendicular to the crystal surface, and incoming and outgoing polarization angles $\psi = 0^{\circ}$ and $\varphi = 0^{\circ}$ are for horizontal orientation of $\mathbf{E}^{\omega,2\omega}$.

TABLE I. List of studied Cu_2O crystals and their parameters.

Sample (No.)	$\mathbf{k}^{\omega} \parallel [\cdots]$	Thickness (μm)
34	[001]	264
33	[001]	45
13	[$\bar{1}$10]	252
29	[11$\bar{2}$]	95
2A	[111]	3874
2B	[11$\bar{2}$]	5103

Cu_2O samples of different orientations are used whose parameters are given in Table I. During experiment they are mounted strain free as described in detail in Ref. [17] and kept in a bath cryostat in superfluid helium at a temperature of $T = 1.4$ K.

In order to illustrate the local dependence of the SHG signals on the sample position, we used a 7× magnifying telescope instead of the focusing lens of the laser on the sample. Thus, a large part of the sample is illuminated. The cross section of the sample is mapped to the CCD chip by opening the monochromator slit to 3 mm and setting its grating to zero order. Therefore, all light is reflected without dispersion by the grating to the CCD camera.

III. EXPERIMENTAL RESULTS

In this section, we present experimental results for Cu_2O crystals of different orientations. In Fig. 3, the spectral range of the yellow exciton series 2.032–2.175 eV is shown with a break from 2.034 to 2.148 eV. Exciton resonances are marked with their principal quantum number and main orbital angular momentum contribution to the envelope [11]. The resonance at 2.155 eV labeled as $1S_g$, is the 1S exciton of the green series, following the assignment of Ref. [22]. Spectra and SHG polarization dependences for an allowed orientation (a) {$\mathbf{k}^{\omega} \parallel [11\bar{2}]$} and a forbidden orientation (b) {$\mathbf{k}^{\omega} \parallel [001]$} are presented. For $\mathbf{k}^{\omega} \parallel [11\bar{2}]$ SHG is allowed, and we find resonances for S- and D excitons of the yellow series. The polarization dependences for the 1S and 3S excitons, however, show clear differences, which give already evidence for different SHG mechanisms for the 1S and the higher resonances. For the forbidden orientation $\mathbf{k}^{\omega} \parallel [001]$ only the 1S resonance of the yellow series is present in the SHG spectrum, whereas the resonances with higher n are absent in accordance with symmetry analysis.

In Fig. 3(a), the linewidth of the yellow 1S resonance has a FWHM of 90 μeV being limited by the setup spectral resolution. Two-photon absorption experiments determined in similar Cu_2O samples with the 1S linewidth of about 1 μeV [17]. All other exciton resonances have larger linewidths not limited by the setup, e.g., the 3S resonance has a FWHM of 290 μeV.

In Fig. 4, we show the rotational anisotropies of the 1S exciton for the four studied crystal directions. SHG signal

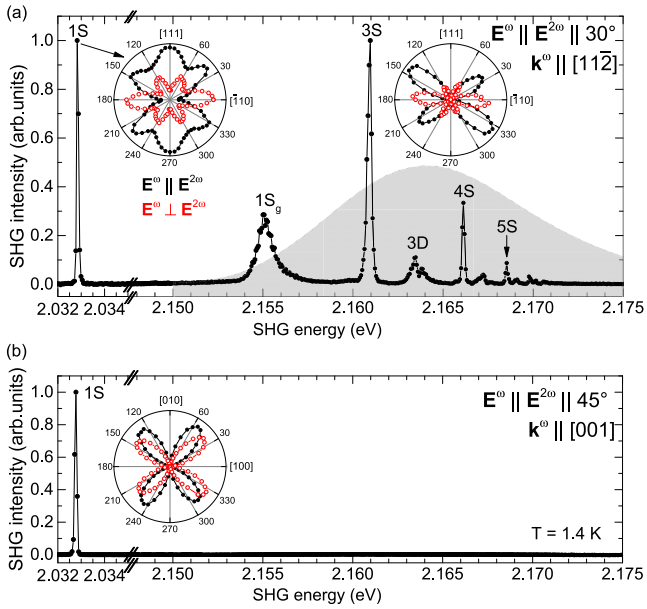

FIG. 3. SHG spectra of Cu_2O for (a) sample No. 29 with $\mathbf{k}^\omega \parallel [11\bar{2}]$ and (b) sample No. 34 with $\mathbf{k}^\omega \parallel [001]$. The laser photon energy is set to 1.016 eV for the 1*S* resonance and to 1.082 eV for the higher exciton resonances. Note the different low- and high-energy scales divided by break lines. The energy range around the 2*S* exciton is not shown here. Exciton line intensities in the higher-energy range are enlarged by a factor of 10 to meet the intensity of the 1*S* line [(a) and (b)]. The SHG peak intensities are not normalized to the laser spectrum (indicated by the gray shaded area). The insets in panel (a) show SHG rotational anisotropies of the 1*S* and 3*S* excitons and in panel (b) for the 1*S* exciton. The other high-*n* excitons show the same rotational anisotropies as the 3*S* exciton. Filled black and open red circles represent data for the $\mathbf{E}^\omega \parallel \mathbf{E}^{2\omega}$ and $\mathbf{E}^\omega \perp \mathbf{E}^{2\omega}$ configurations, respectively.

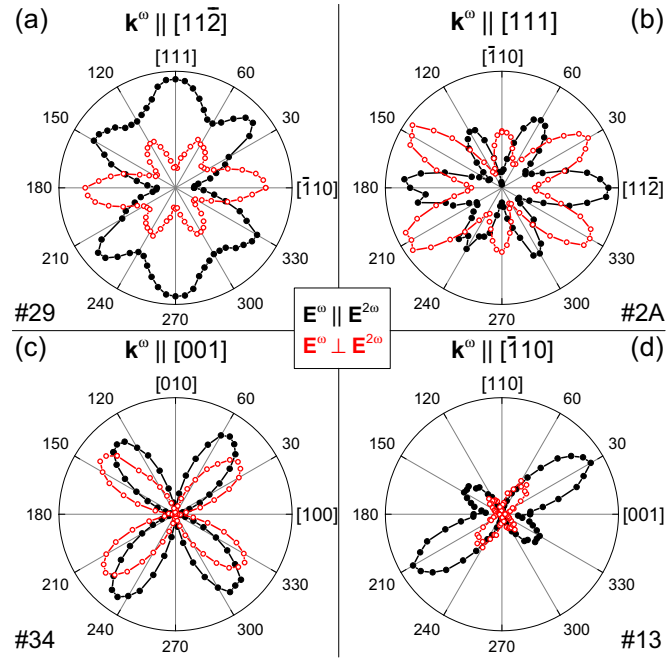

FIG. 4. SHG rotational diagrams of the 1*S* exciton at 2.0328 eV in four crystal directions: (a) and (b) refer to results in allowed directions, whereas (c) and (d) refer to forbidden directions. Filled black and open red dots refer to parallel and perpendicular polarizations, respectively, of in- and outgoing photons. Sample numbers are given by number.

intensities in forbidden and allowed directions are of the same order of magnitude, but angular dependencies are quite different.

For the 1*S* resonance in one exemplary forbidden direction ($\mathbf{k}^\omega \parallel [\bar{1}10]$), we found out that the SHG signal strength as well as the polarization diagram depend on the position of the laser focus on the sample. Thus, we suggest that local strain [23] is the reason for symmetry breaking and the appearance of the SHG signal at the 1*S* exciton. To test this hypothesis, we measured spatially resolved SHG of the yellow 1*S* resonance at 2.0328 eV. The SHG signal of the whole sample area 3×3 mm^2 is shown in Fig. 5. The color map corresponds to SHG intensity. Two SHG spots on the sample, denoted by a and b, are chosen, and their rotational anisotropies are plotted in Fig. 6. As will be confirmed by our model analysis in Sec. VI, the appearance of SHG signal for $\mathbf{k}^\omega \parallel [\bar{1}10]$ and the differences in polarization dependences at various spots are induced due to local strains of different amplitudes and orientations.

To prove this assumption of local strain as SHG origin and gain insight into the strain parameters, such as the strain tensor components, we simulate the experimental rotational anisotropies. Our model and the fitting procedure are described below.

IV. THEORY

In this section, we extend our derivation of polarization dependences as outlined in detail in Ref. [14] to include strain-induced perturbations and band-structure higher-order effects. It explains the experimental findings of unexpected SHG by the presence of residual strain in the Cu_2O samples.

More specifically, the formalism includes the **k**-dependent splitting of the 1*S* longitudinal and transversal components,

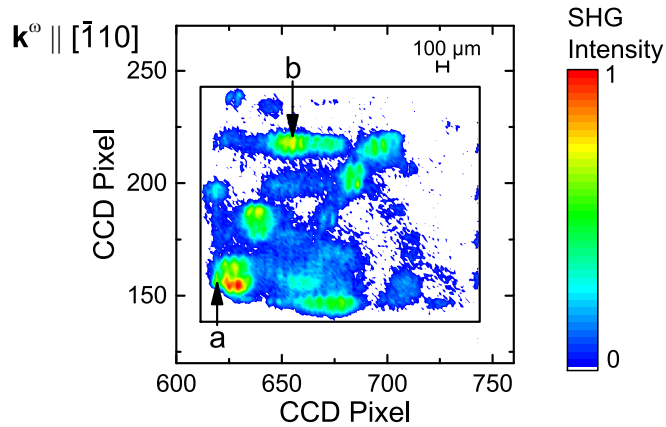

FIG. 5. Spatially resolved 1*S* SHG image of sample No. 13 in a forbidden orientation ($\mathbf{k}^\omega \parallel [\bar{1}10]$) at 2.0328 eV. Observed SHG signals are induced by local strains. The area shown corresponds to 3×3 mm^2. At spots a and b rotational anisotropies are measured for comparison and shown in Fig. 6.

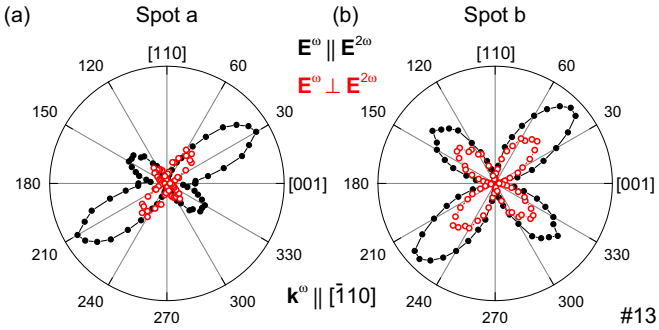

FIG. 6. SHG rotational anisotropies of the yellow 1*S* exciton at 2.0328 eV for spots a and b of sample No. 13 with $\mathbf{k}^{\omega} \parallel [\bar{1}10]$ as marked in Fig. 5. Filled black and open red dots mark data points of parallel and crossed configurations, respectively.

which is explained as an effect of the band structure in Ref. [23]. It also considers the mixing of these components by local strain. We start with presenting the main concepts in four steps that we need for the simulation of our experimental results in Sec. V.

A. Photon operators

For the analysis of SHG signals on exciton resonances, we start with the relevant definitions as shown in Fig. 2. The ingoing photons are described by their wave-vector $\mathbf{k}^{\omega}$ and polarization $\mathbf{E}^{\omega}$. The polarization components u, v, and w depend on the incoming polarization angle ψ. Emitted photons have wave-vector $\mathbf{k}^{2\omega}$ with components k_x, k_y, k_z, and polarization $\mathbf{E}^{2\omega}$. The polarization components m, n, and o depend on the outgoing polarization angle φ,

$$\mathbf{E}^{\omega} = \begin{pmatrix} u(\psi) \\ v(\psi) \\ w(\psi) \end{pmatrix}, \quad \mathbf{E}^{2\omega} = \begin{pmatrix} m(\varphi) \\ n(\varphi) \\ o(\varphi) \end{pmatrix}, \quad \mathbf{k}^{2\omega} = \begin{pmatrix} k_x \\ k_y \\ k_z \end{pmatrix}. \tag{1}$$

Note that $\mathbf{k}^{\omega}$ and $\mathbf{k}^{2\omega}$ are parallel and $\mathbf{k}^{2\omega}$ is twice as large as $\mathbf{k}^{\omega}$. The k_i's applied in the calculations are unit direction vector components. As outlined in detail in Ref. [14], *S*/*D* excitons of even parity are two-photon dipole allowed. Their polarization-dependent excitation is described by the two-photon dipole-dipole (TPDD) operator,

$$O_{\mathrm{TPDD}}(\mathbf{E}^{\omega}) = \sqrt{2} \begin{pmatrix} v(\psi)w(\psi) \\ u(\psi)w(\psi) \\ u(\psi)v(\psi) \end{pmatrix} = \begin{pmatrix} x \\ y \\ z \end{pmatrix}. \tag{2}$$

The quadrupole operator as an even-parity operator leads to the emission of the outgoing photons,

$$O_{\mathrm{Q}}(\mathbf{k}^{2\omega}, \mathbf{E}^{2\omega}) = \frac{1}{\sqrt{2}} \begin{pmatrix} k_y o(\varphi) + k_z n(\varphi) \\ k_z m(\varphi) + k_x o(\varphi) \\ k_x n(\varphi) + k_y m(\varphi) \end{pmatrix}. \tag{3}$$

The intensity of the SHG signal is given by

$$I^{2\omega} \propto |(O_{\mathrm{TPDD}} O_{\mathrm{Q}})|^2. \tag{4}$$

If Eq. (4) is calculated for the $\mathbf{k}^{\omega}$ directions of the laser light used in this paper, SHG is expected only for low-symmetry crystal directions as, e.g., [111] and $[11\bar{2}]$, whereas it is forbidden for $\mathbf{k}^{\omega} \parallel [001]$ and $\mathbf{k} \parallel [\bar{1}10]$.

In this paper, we show that Eq. (4) needs modification to explain the experimental results for the 1*S* exciton in both the allowed and the forbidden directions.

B. k^2-dependent splitting of the 1*S* exciton

The 1*S* orthoexciton is known for a small wave-vector-dependent splitting of its longitudinal and transversal components showing up in high-resolution transmission measurements [17]. This splitting is explained by a coupling between the Γ_7^+ and the Γ_8^+ valence bands leading to an anisotropic exciton mass of the three exciton states [23]. It was shown in Ref. [17] that the splitting for one-photon excitation can be consistently described by two parameters $\Delta_3 = -1.3$ and $\Delta_5 = 2$ μeV. Calculations by Schweiner *et al.* [23] yield the slightly different values of $\Delta_3 = -1.45$ and $\Delta_5 = 1.96$ μeV.

For two-photon excitation, however, $2\mathbf{k}^{\omega} < \mathbf{k}_0$ (wave number at one-photon resonance). From the polariton dispersion, we estimate $\Delta_{3,(5)}(\mathbf{k}^{2\omega}) \sim 0.8\Delta_{3,(5)}(\mathbf{k}_0)$, which are the values used in our calculations in the following. The k^2 matrices are given in Refs. [17,23],

$$J_3 = \Delta_3 \begin{pmatrix} 3k_x^2 - k^2 & 0 & 0 \\ 0 & 3k_y^2 - k^2 & 0 \\ 0 & 0 & 3k_z^2 - k^2 \end{pmatrix}, \tag{5}$$

and

$$J_5 = \Delta_5 \begin{pmatrix} 0 & k_x k_y & k_x k_z \\ k_x k_y & 0 & k_y k_z \\ k_x k_z & k_y k_z & 0 \end{pmatrix}. \tag{6}$$

From these matrices, we can, on one hand, determine the modification of the exciton states by the $\boldsymbol{k}^2$ term and, on the other hand, the impact on the photon operators determining the SHG. From the structure of the matrices, it is obvious that J_3 shifts the exciton components, leading to a splitting, but does not induce state mixing. Consequently, also the components of the photon operators remain unconnected when J_3 acts on them.

Mixing can be achieved through J_5 which depends, however, strongly on the direction in k space. Along the SHG-forbidden direction [001], it is suppressed, whereas along $[\bar{1}10]$, the transverse components of the photon operators along x and y remain disconnected from the longitudinal component along z. The consequences for SHG will be discussed below. Along the directions of even lower symmetry for which SHG is allowed anyway, J_5 modifies the mixing of the photon operator components involved in the process.

C. Strain tensors

The strain is described by matrices M_3 and M_5 of the same structure as J_3 and J_5 in Eqs. (5) and (6). The uniaxial strain that can lift the degeneracy of states without mixing them is given by M_3,

$$M_3 = \delta_3 \begin{pmatrix} \epsilon_x & 0 & 0 \\ 0 & \epsilon_y & 0 \\ 0 & 0 & \epsilon_z \end{pmatrix}, \tag{7}$$

with $\epsilon_i = 3\epsilon_{ii}^2 - \frac{1}{3}(\epsilon_{xx}^2 + \epsilon_{yy}^2 + \epsilon_{zz}^2)$.

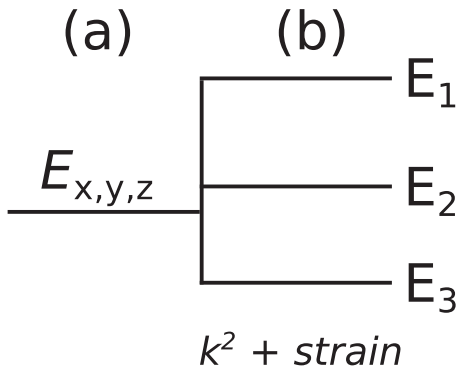

FIG. 7. General splitting of the exciton components. (a) Unperturbed exciton states $E_{x,y,z}$. (b) New exciton eigenstates E_{1-3}, split in energy and mixed by the k^2 and strain terms.

Matrix M_5 represents the shear strain which can mix exciton components,

$$M_5 = \delta_5 \begin{pmatrix} 0 & \epsilon_{xy} & \epsilon_{xz} \\ \epsilon_{xy} & 0 & \epsilon_{yz} \\ \epsilon_{xz} & \epsilon_{yz} & 0 \end{pmatrix}. \tag{8}$$

ϵ_{ij}'s are the strain tensor components. For the deformation potentials δ_i, we use the hydrostatic strain $\delta_3 = -0.29$ eV and shear strain $\delta_5 = 0.18$ eV given in Ref. [24].

Summarizing these additional factors, a splitting of the exciton components can be induced by the strain and the k^2 term as schematically shown in Fig. 7(b). It is, however, *a priori* not possible to estimate whether one effect dominates the other or one effect can be treated as a small perturbation compared to the other. Therefore, the sum matrix S, Eq. (9), of both needs to be diagonalized

$$S = J_3 + J_5 + M_3 + M_5. \tag{9}$$

Turning to the impact on SHG, generally, S can couple the components x, y, and z of the two-photon excitation operator O_{TPDD}, Eq. (2). This coupling results in new components x', y', and z' of O'_{TPDD} allowing for new SHG contributions,

$$O'_{\mathrm{TPDD}} = S O_{\mathrm{TPDD}}. \tag{10}$$

We note that the J_i and M_i have the dimension energy, so the formally O' and O have different dimensions. In the SHG calculations, the intensity is scaled by proportionality factors, which adjust the dimension correspondingly.

D. Calculation of strain-induced SHG

We consider only the three 1S orthoexciton components of Γ_5^+ symmetry. The first requirement for strain-induced SHG is the two-photon excitation of components mixed by the strain. In a second step emission by one photon in quadrupole order has to be allowed to observe the SHG signal. Therefore, in Eq. (11), SHG including both strain and band effects is calculated by

$$I^{2\omega}_{\mathrm{perturb}} \propto |O'_{\mathrm{TPDD}} O_{\mathrm{Q}}|^2. \tag{11}$$

The scalar product in Eq. (11) with the components of O'_{TPDD}, d_i and those of O_{Q}, q_j needs further investigation to work out our theoretical concept. Its general form is given by

$$\begin{pmatrix} d_1 \\ d_2 \\ d_3 \end{pmatrix} \begin{pmatrix} q_1 \\ q_2 \\ q_3 \end{pmatrix} = d_1 q_1 + d_2 q_2 + d_3 q_3 := a_1 + a_2 + a_3. \tag{12}$$

Thus, the SHG intensity, i.e., the square of Eq. (12), can be divided into two parts,

$$(a_1 + a_2 + a_3)^2 = \underbrace{(a_1^2 + a_2^2 + a_3^2)}_{I^{2\omega}_{\mathrm{add}}} + \underbrace{2(a_1 a_2 + a_2 a_3 + a_1 a_3)}_{I^{2\omega}_{\mathrm{int}}}. \tag{13}$$

The first three terms are insensitive to the relative phases as each component is squared by itself. The second part depends on the relative phases of the three components and their interferences. In general, all components will contribute to SHG. However, if the exciton level splittings induced by the k^2 and strain tensor components exceed the exciton linewidths, the interference term vanishes.

The total (normalized) SHG signal can thus be decomposed in the following way using the scaling parameters a and b ($a + b = 1$):

$$I^{2\omega}_{\mathrm{SHG}} = a I^{2\omega}_{\mathrm{add}} + b I^{2\omega}_{\mathrm{int}}. \tag{14}$$

The fitting result for the scaling parameters a and b allows us to determine the ratios of both contributions.

V. MODELING

In this section, we present the results of our simulations for the four crystal directions studied experimentally on the yellow 1S exciton resonance, considering first the directions along which SHG is nominally forbidden before turning to the SHG-allowed cases.

A. SHG for $\mathbf{k}^{\omega} \parallel$ [001]

We start with the crystal direction of highest symmetry ($\mathbf{k}^{\omega} \parallel [001]$). For this crystal orientation, the exciton components are oriented along

$$\mathbf{z} = \begin{pmatrix} 0 \\ 0 \\ 1 \end{pmatrix}, \quad \mathbf{x} = \begin{pmatrix} 1 \\ 0 \\ 0 \end{pmatrix}, \quad \mathbf{y} = \begin{pmatrix} 0 \\ 1 \\ 0 \end{pmatrix}. \tag{15}$$

The polarization of the ingoing photons is as follows:

$$\mathbf{E}^{\omega} = \begin{pmatrix} \cos\psi \\ \sin\psi \\ 0 \end{pmatrix}. \tag{16}$$

The two-photon operator according to Ref. [15] is given by

$$O_{\mathrm{TPDD}}(\mathbf{E}^{\omega}) = \frac{1}{\sqrt{2}} \begin{pmatrix} 0 \\ 0 \\ \sin(2\psi) \end{pmatrix}. \tag{17}$$

Subsequent emission by the quadrupole operator O_{Q} Eq. (18) is only possible from the $\mathbf{x}$ and $\mathbf{y}$ components of the exciton,

$$O_{\mathrm{Q}}(\mathbf{k}^{2\omega}, \mathbf{E}^{2\omega}) = \frac{1}{\sqrt{2}} \begin{pmatrix} \sin\varphi \\ \cos\varphi \\ 0 \end{pmatrix}. \tag{18}$$

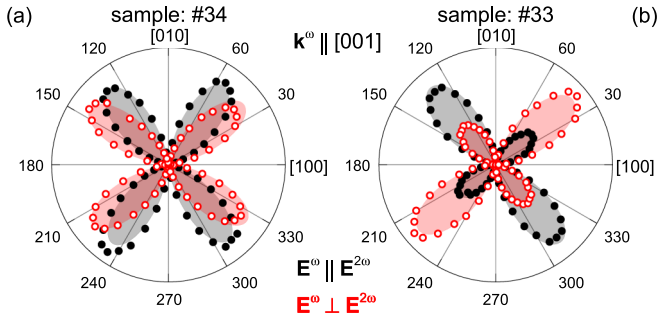

FIG. 8. Experimental data and simulation of the anisotropies for the 1*S* exciton ($\mathbf{k}^\omega \parallel [001]$) of (a) sample No. 34 and (b) sample No. 33. Filled black and open red dots mark data points of polarization dependences for the geometries $\mathbf{E}^\omega \parallel \mathbf{E}^{2\omega}$ and $\mathbf{E}^\omega \perp \mathbf{E}^{2\omega}$. Gray and red shaded areas show the results of fits to the data.

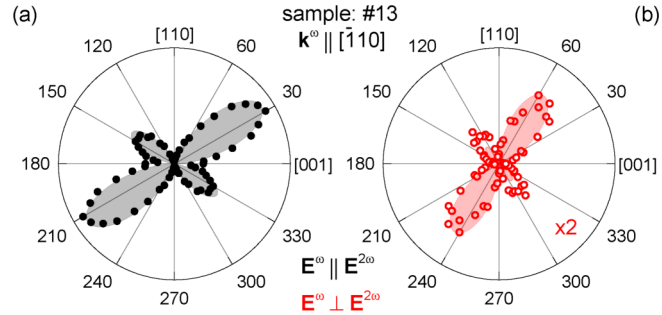

FIG. 9. Simulation and data of the anisotropies for the 1*S* exciton ($\mathbf{k}^\omega \parallel [\bar{1}10]$) in sample No. 13. Filled black and open red dots give data points of polarization dependences for (a) the geometries $\mathbf{E}^\omega \parallel \mathbf{E}^{2\omega}$ and (b) $\mathbf{E}^\omega \perp \mathbf{E}^{2\omega}$. Gray and red shaded areas show the result of the fits to the data.

Because both operators [Eqs. (17) and (18)] address different exciton components, no SHG is expected along this high-symmetry direction according to Eq. (4) in the unstrained crystal.

If only the k^2 terms [Eqs. (5) and (6)] are considered, the J_3 matrix partially lifts the exciton degeneracy. The two transverse exciton components remain degenerate and are split from the longitudinal component [17,23]. The J_5 matrix vanishes for the $\mathbf{k}^\omega \parallel [001]$ orientation so that it does not lead to state mixing required for SHG.

Finally, we account also for the influence of strain. Applying the matrix S [Eq. (9)] to the excitation operator O_{TPDD}, it is transformed into O'_{TPDD} [Eq. (10)] with the components,

$$x' = \delta_5 \epsilon_{xz} z, \quad y' = \delta_5 \epsilon_{yz} z, \quad z' = (2\Delta_3 + \delta_3 \epsilon_z) z. \tag{19}$$

Now, SHG becomes obviously allowed as the only component z that can be excited by two photons is coupled by strain to the components x' and y' from which quadrupole emission is possible. Through measuring the SHG, one may assess the shear strain components ϵ_{xz} and ϵ_{yz}, whereas other strain components remain unknown.

In Fig. 8, we present measurements on two samples (No. 34 and No. 33) with $\mathbf{k}^\omega \parallel [001]$ and corresponding fits with Eq. (14) to the data. The anisotropy diagram of sample No. 34 [Fig. 8(a)] reveals a fourfold symmetric signal. The fit is performed with the parameter values given in Table II. Despite the same orientation of sample No. 33 shown in Fig. 8(b), the rotational diagram has a different shape as compared to No. 34 [Fig. 8(a)].

The fits indicate that the exciton states have a large splitting compared to their linewidths so that the interference terms are weak as $a \gg b$. The shear strain, which is the origin of the SHG, is much larger for sample No. 34 than for No. 33, despite its higher-symmetry SHG pattern.

TABLE II. Simulation fit parameters [ϵ_i and ϵ_{ij} given in units of (10^{-6})] for samples No. 34 and No. 33, according to Eq. (14). Entries (—) indicate that this parameter cannot be obtained in this $\mathbf{k}^\omega$ direction.

Sample (No.)	a	b	ϵ_x	ϵ_y	ϵ_z	ϵ_{xy}	ϵ_{xz}	ϵ_{yz}
34	0.98	0.02	–	–	–	–	23	10
33	0.73	0.27	–	–	–	–	−2.4	−2.4

B. SHG for $\mathbf{k}^\omega \parallel [\bar{1}10]$

For $\mathbf{k}^\omega \parallel [\bar{1}10]$ the corresponding crystal directions are as follows:

$$\mathbf{z} = \frac{1}{\sqrt{2}}\begin{pmatrix}-1\\1\\0\end{pmatrix}, \quad \mathbf{x} = \begin{pmatrix}0\\0\\1\end{pmatrix}, \quad \mathbf{y} = \frac{1}{\sqrt{2}}\begin{pmatrix}1\\1\\0\end{pmatrix}. \tag{20}$$

The polarization of the photons is given by

$$\mathbf{E}^\omega = \frac{1}{\sqrt{2}}\begin{pmatrix}\sin\psi\\ \sin\psi\\ \sqrt{2}\cos\psi\end{pmatrix}. \tag{21}$$

Therefore, the operators for excitation and emission are given by

$$O_{\mathrm{TPDD}}(\mathbf{E}^\omega) = \begin{pmatrix}\cos\psi\sin\psi\\ \cos\psi\sin\psi\\ \frac{1}{\sqrt{2}}\sin^2\psi\end{pmatrix}, \tag{22}$$

and

$$O_{\mathrm{Q}}(\mathbf{k}^{2\omega}, \mathbf{E}^{2\omega}) = \frac{1}{2}\begin{pmatrix}\cos\varphi\\ -\cos\varphi\\ 0\end{pmatrix}. \tag{23}$$

For this $\mathbf{k}^\omega$ direction, the combined action of the J_3 and J_5 matrices completely lifts the degeneracy of the exciton components. Still, SHG remains impossible without strain as the longitudinal and transversal components remain independent. SHG is induced also here by shear strain resulting in the required mixing. Since emission is not possible through the z' component in which ϵ_z exclusively appears, this strain parameter cannot be evaluated in this geometry. However, the reduced symmetry compared to the previous case gives access to all other strain components.

In Fig. 9, we present measurements on sample No. 13 with $\mathbf{k}^\omega \parallel [\bar{1}10]$ and corresponding fitting with Eq. (14) to the experimental data.

The results from the fitting procedure for the parameters are summarized in Table III. Remarkably, a and b are of the same order of magnitude so that the interference term $I^{2\omega}_{\mathrm{int}}$ is

TABLE III. Simulation fit parameters [ϵ_i and ϵ_{ij} given in units of (10^{-6})] for sample No. 13 according to Eq. (14). Entries (—) indicate that this parameter cannot be obtained in this $\mathbf{k}^{\omega}$ direction.

Sample	a	b	ϵ_x	ϵ_y	ϵ_z	ϵ_{xy}	ϵ_{xz}	ϵ_{yz}
No. 13	0.46	0.54	−5.9	−1.9	–	14	4.9	2.7

as important as the one from the individual components $I^{2\omega}_{\text{add}}$. The uniaxial and shear strain parameters are of comparable magnitude, ranging from a few to more than ten parts per 10^6.

C. SHG for $\mathbf{k}^{\omega} \parallel [11\bar{2}]$

For $\mathbf{k}^{\omega} \parallel [11\bar{2}]$, the corresponding crystal directions are as follows:

$$\mathbf{z} = \frac{1}{\sqrt{6}}\begin{pmatrix}1\\1\\-2\end{pmatrix}, \quad \mathbf{x} = \frac{1}{\sqrt{2}}\begin{pmatrix}-1\\1\\0\end{pmatrix}, \quad \mathbf{y} = \frac{1}{\sqrt{3}}\begin{pmatrix}1\\1\\1\end{pmatrix}. \tag{24}$$

This direction differs from the previous ones because here SHG is allowed already without strain. Therefore, $I^{2\omega}$ in Eq. (4) does not vanish. Still, the orthoexciton states are mixed and shifted by k^2 terms and strain leading to a modified SHG signal. This is adequately described by $I^{2\omega}_{\text{add}}$ and $I^{2\omega}_{\text{int}}$.

The polarization of the photons is given by

$$\mathbf{E}^{\omega} = \frac{1}{\sqrt{3}}\begin{pmatrix}-\sqrt{\frac{3}{2}}\cos\psi + \sin\psi\\ \sqrt{\frac{3}{2}}\cos\psi + \sin\psi\\ \sin\psi\end{pmatrix}. \tag{25}$$

The operators for excitation and emission are as follows:

$$O_{\text{TPDD}}(\mathbf{E}^{\omega}) = \frac{1}{3}\begin{pmatrix}\sin\psi(\sqrt{3}\cos\psi + \sqrt{2}\sin\psi)\\ \sin\psi(-\sqrt{3}\cos\psi + \sqrt{2}\sin\psi)\\ -[1+5\cos(2\psi)]/2\sqrt{2}\end{pmatrix}, \tag{26}$$

and

$$O_{\text{Q}}(\mathbf{k}^{2\omega}, \mathbf{E}^{2\omega}) = \frac{1}{6}\begin{pmatrix}-\sqrt{6}\cos\varphi - \sin\varphi\\ \sqrt{6}\cos\varphi - \sin\varphi\\ 2\sin\varphi\end{pmatrix}. \tag{27}$$

Along this low-symmetry direction, both the k^2 and the strain contributions to S mix all three exciton components and modify the SHG. As a consequence, the rotational anisotropy patterns should give insight into all components of the strain tensor. The measured data and the corresponding fits are shown in Fig. 10 and compared to the simulation of the expected anisotropies in the absence of local strain. The parameters from the fits are given in Table IV.

For the studied sample, interference effects are of minor relevance due to a rather large exciton level splitting. The strain components are of comparable magnitude with a few parts per 10^6. The comparison to the case of strain-free SHG shows particularly pronounced deviations, namely, six lobes instead of four lobes in the geometry $\mathbf{E}^{\omega} \parallel \mathbf{E}^{2\omega}$.

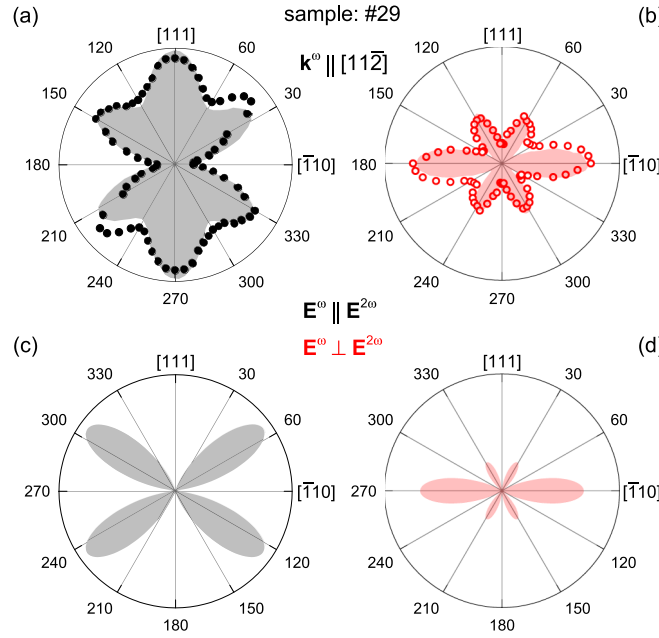

FIG. 10. Simulation and data of the anisotropies for the 1S exciton in sample No. 29 ($\mathbf{k}^{\omega} \parallel [11\bar{2}]$). Filled black and open red dots give data points of polarization dependences for (a) the geometries $\mathbf{E}^{\omega} \parallel \mathbf{E}^{2\omega}$ and (b) $\mathbf{E}^{\omega} \perp \mathbf{E}^{2\omega}$. Gray and red shaded areas show the result of the fits to the data. In (c) and (d), the parallel and perpendicular geometries, respectively, are simulated in the absence of local strain, according to Eq. (4).

D. SHG for $\mathbf{k}^{\omega} \parallel [111]$

This k direction is similar to $\mathbf{k}^{\omega} \parallel [11\bar{2}]$ since all three terms of Eq. (14) are allowed. For $\mathbf{k}^{\omega} \parallel [111]$, the corresponding crystal directions are as follows:

$$\mathbf{z} = \frac{1}{\sqrt{3}}\begin{pmatrix}1\\1\\1\end{pmatrix}, \quad \mathbf{x} = \frac{1}{\sqrt{6}}\begin{pmatrix}1\\1\\-2\end{pmatrix}, \quad \mathbf{y} = \frac{1}{\sqrt{2}}\begin{pmatrix}-1\\1\\0\end{pmatrix}. \tag{28}$$

The polarization of the photons is given by

$$\mathbf{E}^{\omega} = \frac{1}{\sqrt{2}}\begin{pmatrix}\frac{1}{\sqrt{3}}\cos\psi - \sin\psi\\ \frac{1}{\sqrt{3}}\cos\psi + \sin\psi\\ -\frac{2}{\sqrt{3}}\cos\psi\end{pmatrix}. \tag{29}$$

Therefore, the operators for excitation and emission are as follows:

$$O_{\text{TPDD}}(\mathbf{E}^{\omega}) = \frac{\sqrt{2}}{3}\begin{pmatrix}\cos\psi(-\cos\psi - \sqrt{3}\sin\psi)\\ \cos\psi(-\cos\psi + \sqrt{3}\sin\psi)\\ -[1+2\cos(2\psi)]/2\end{pmatrix}, \tag{30}$$

TABLE IV. Simulation fit parameters [ϵ_i and ϵ_{ij} given in units of (10^{-6})] for sample No. 29, according to Eq. (14).

Sample	a	b	ϵ_x	ϵ_y	ϵ_z	ϵ_{xy}	ϵ_{xz}	ϵ_{yz}
No. 29	0.87	0.13	2.1	2.0	−1.4	−1.3	0.14	−0.24

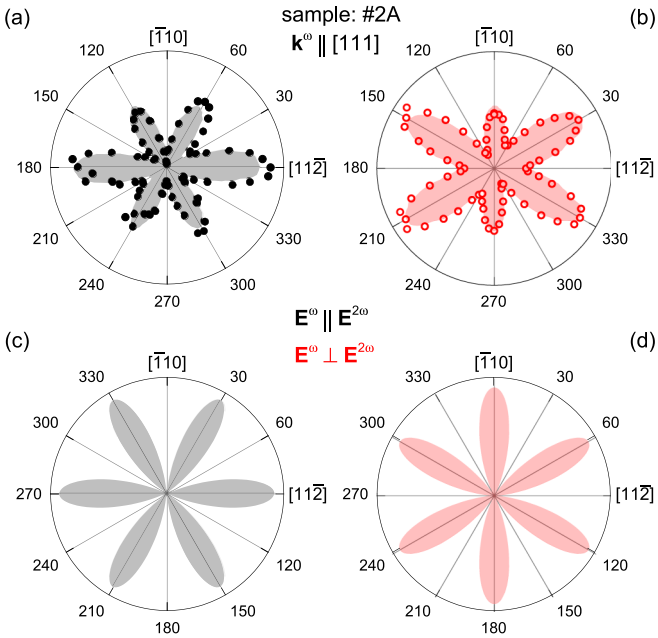

FIG. 11. Simulation and data of the anisotropies for the 1*S* exciton in sample No. 2A ($\mathbf{k}^{\omega} \parallel [111]$). Filled black and open red dots indicate data points of polarization dependences for (a) the geometries $\mathbf{E}^{\omega} \parallel \mathbf{E}^{2\omega}$ and (b) $\mathbf{E}^{\omega} \perp \mathbf{E}^{2\omega}$. Gray and red shaded areas show the result of the fits to the data. In (c) and (d), the parallel and perpendicular geometries, respectively, are simulated in the absence of local strain, according to Eq. (4).

and

$$O_{\mathrm{Q}}(\mathbf{k}^{2\omega}, \mathbf{E}^{2\omega}) = \frac{1}{6}\begin{pmatrix} -\cos\varphi + \sqrt{3}\sin\varphi \\ -\cos\varphi - \sqrt{3}\sin\varphi \\ 2\cos\varphi \end{pmatrix}. \tag{31}$$

Measured data and best fits for sample No. 2A with $\mathbf{k}^{\omega} \parallel [111]$ are depicted in Fig. 11. In addition, simulated anisotropies in the absence of local strain are shown. Parameters from the fit are listed in Table V. As in sample No. 29 with $\mathbf{k}^{\omega} \parallel [11\bar{2}]$, contribution *a* dominates due to rather large energy-level splitting. The interference is of minor importance.

In contrast to the previous case, the local strain does not lead to fundamental changes in the SHG pattern appearance but influences mostly the intensity values along the different directions.

VI. DISCUSSION

After analyzing and fitting the SHG signal in two forbidden and two allowed crystal directions, we turn to a discussion of some details. By the fitting, the strain tensor components ϵ_i and ϵ_{ij} have been determined. However, along the two high-symmetry directions and along $\mathbf{k}^{\omega} \parallel [11\bar{2}]$, the parameter set is incomplete, whereas for the low-symmetry direction $\mathbf{k}^{\omega} \parallel [111]$, all parameters are known. In this case, the full matrix *S* in Eq. (9) can be diagonalized. Its eigenvalues E_i give the energy shifts, induced by the k^2 terms and the strain, relative to the idealized situation with a degenerate orthoexciton state. The new eigenvectors $\boldsymbol{v}_i$ indicate the mixing strength of the original states. The eigenvalues and eigenvectors for every sample are summarized in Table VI. From these data, we can, in particular, reassess the importance of the interference term based on the magnitude of the exciton level splitting compared to the 1*S* linewidth, which, so far, was concluded indirectly only through the relative magnitude of *a* and *b* but now can be quantified directly.

Despite the incomplete parameters' set, we consider also the case $\mathbf{k}^{\omega} \parallel [001]$ for samples No. 34 and No. 33 for illustration, even though for these two samples the unknown strain components might influence the energy splitting and level mixing. As discussed, $\boldsymbol{v}_1$ and $\boldsymbol{v}_2$ with their admixture of $\mathbf{z}$ are excited by two photons through this component and emit by their components $\mathbf{x}$ and $\mathbf{y}$. Eigenvector $\boldsymbol{v}_3$ is not involved in the SHG generation. The energy splitting between $\boldsymbol{v}_1$ and $\boldsymbol{v}_2$ is of importance regarding their degree of interference. According to the eigenvalues E_1 and E_2 for sample No. 34 (Table VI), the splitting is 10 μeV. With the 1*S* linewidth of 1 μeV [17], it is obvious that both states are sufficiently split in energy to neglect interference. This is supported by the fitting result $a = 0.98$, showing the large contribution of $I^{2\omega}_{\mathrm{add}}$. In the case of sample No. 33, the degree of mixing between $\mathbf{z}$ and the other two components is smaller, but still $\boldsymbol{v}_1$ and $\boldsymbol{v}_2$ contain an admixture of $\mathbf{z}$. The splitting of these two eigenstates E_1 and E_2 is 4.5 μeV so that interference may still play some role. The ratio of *a* and *b* suggests that one quarter of the SHG signal originates from $I^{2\omega}_{\mathrm{int}}$.

For $\mathbf{k}^{\omega} \parallel [\bar{1}10]$, sample No. 13, the new eigenvectors $\boldsymbol{v}_1$ and $\boldsymbol{v}_3$ have an admixture of $\mathbf{z}$ that allows for quadrupole emission. According to the fit, these are split in energy by 2.1 μeV only so that the SHG signal shows almost equal contributions from $I^{2\omega}_{\mathrm{add}}$ and $I^{2\omega}_{\mathrm{int}}$.

TABLE V. Simulation fit parameters [ϵ_i and ϵ_{ij} given in units of (10^{-6})] for sample No. 2A, according to Eq. (14).

Sample	*a*	*b*	ϵ_x	ϵ_y	ϵ_z	ϵ_{xy}	ϵ_{xz}	ϵ_{yz}
No. 2A	0.79	0.21	−5.0	−2.0	−1.4	0.02	0.28	0.37

TABLE VI. Eigenenergies E_i given in units of (μeV) and eigenvectors $\boldsymbol{v}_i$ deduced from the fitting for all samples under investigation.

$\mathbf{k}^{\omega} \parallel [\cdots]$	[001]		[$\bar{1}$10]	[11$\bar{2}$]	[111]
Sample	No. 34	No. 33	No. 13	No. 29	No. 2A
E_1	−5.8	−3.0	2.8	3.8	−7.3
E_2	4.4	1.5	−1.3	−3.1	2.1
E_3	1.5	1.5	0.72	2.0	−1.1
$\boldsymbol{v}_1$	$\begin{pmatrix}0.24\\0.04\\0.72\end{pmatrix}$	$\begin{pmatrix}0.01\\0.01\\0.98\end{pmatrix}$	$\begin{pmatrix}0.45\\0.20\\0.35\end{pmatrix}$	$\begin{pmatrix}0.51\\0.49\\0.00\end{pmatrix}$	$\begin{pmatrix}0.96\\0.03\\0.01\end{pmatrix}$
$\boldsymbol{v}_2$	$\begin{pmatrix}0.61\\0.11\\0.28\end{pmatrix}$	$\begin{pmatrix}0.50\\0.48\\0.02\end{pmatrix}$	$\begin{pmatrix}0.34\\0.66\\0.00\end{pmatrix}$	$\begin{pmatrix}0.01\\0.03\\0.96\end{pmatrix}$	$\begin{pmatrix}0.03\\0.49\\0.48\end{pmatrix}$
$\boldsymbol{v}_3$	$\begin{pmatrix}0.15\\0.85\\0.00\end{pmatrix}$	$\begin{pmatrix}0.49\\0.51\\0.00\end{pmatrix}$	$\begin{pmatrix}0.21\\0.14\\0.65\end{pmatrix}$	$\begin{pmatrix}0.48\\0.48\\0.04\end{pmatrix}$	$\begin{pmatrix}0.01\\0.48\\0.51\end{pmatrix}$

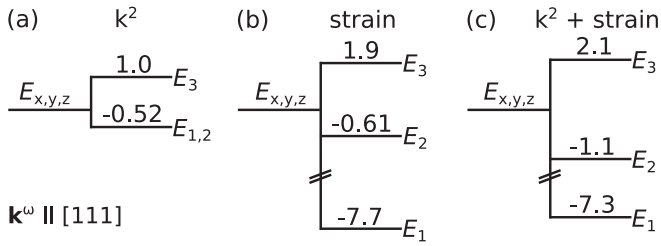

FIG. 12. Energy splitting (μeV) of the three 1S orthoexciton components for $\mathbf{k}^{\omega} \parallel [111]$ by (a) the k^2 term, (b) the strain term, and (c) both the k^2 and the strain terms.

For the SHG allowed $\mathbf{k}^{\omega}$ directions $[11\bar{2}]$ and [111], the situation is more intricate. The k^2 and strain terms lead to new eigenvectors all of which resemble admixtures of all three components. In both directions, therefore, all three exciton components can be excited by two photons and can emit by a quadrupole order photon. Therefore, the SHG contributions to $I^{2\omega}_{\text{add}}$ and $I^{2\omega}_{\text{int}}$ cannot be identified as clearly as for the *a priori* SHG forbidden directions.

However, more insight can be achieved from the energy splittings. We discuss as an example sample No. 2A with $\mathbf{k}^{\omega} \parallel [111]$ for which all strain tensor components ϵ_i and ϵ_{ij} are known from the fit to the rotational anisotropies so that the diagonalization of matrix S delivers the complete information. The relative splittings are about 9 μeV between two states 1 and 2, and 6 μeV between states 1 and 3 so that the corresponding interferences can be neglected, whereas the one between state 2 and state 3 (3.2 μeV) is of importance.

Knowing all contributions to k^2 and strain terms in matrix S in this case, we can also separate them by hand in order to understand their influence on the exciton level splitting. In Fig. 12, we show calculations for splitting by the k^2 term alone by the strain term alone and by including both factors. From this pattern, it becomes clear that for this sample the strain being on the order of 10^{-6} is dominating the k^2 terms which are on the order of a μeV. From the deformation potentials, it is clear that strain components have to be below 10^{-6} to lead to comparable or smaller energy-level shifts. For this sample, the strain is a few parts per 10^6 and thus is more important than the effect of the k^2 terms. One also sees that the k^2 and strain energy shifts do not simply add up because the total shifts are smaller in magnitude than those by strain alone.

For sample No. 29, the three exciton states are distributed over an energy range of about 7 μeV. It is slightly less than for sample No. 2A so that a similar situation concerning the interference of the contributions from the different states is expected. Adjacent states overlap leading to slightly more enhanced interference, whereas the two outermost states are almost independent.

Let us turn now to the disappearance of SHG from the higher-lying excitons along the symmetry forbidden directions even though they are also exposed to strain. We explain the difference between the 1S exciton and the excitons of higher principal quantum number n by the ratios of the energy splitting of the components and their lifetimes. By k^2 and strain, new two-photon dipole and one-photon quadrupole allowed eigenstates are induced. The crucial point is the phase relation between these states. In the moment of femtosecond excitation, no SHG can be observed due to interference of the new eigenstates. After time t, the phase relation between the new eigenstates at $E_i = \hbar\omega_i$ and $E_j = \hbar\omega_j$ has changed by $|\omega_j - \omega_i|t = \Delta\omega\, t$ and allows for detecting SHG. This change in phase is possible only if the lifetime τ of the involved states is much longer than $1/\Delta\omega$. Therefore, the inequality,

$$\tau\, \Delta\omega \gg 1 \tag{32}$$

applies. From the 1S exciton linewidth of less than 1 μeV [17], its lifetime is calculated to $\tau = 1.3$ ns. The k^2 and strain energy splitting $\Delta\omega$ from the fits are 10, 4.5, and 2.1 μeV for samples No. 34, No. 33, and No. 13, respectively. These values are underestimated as certain strain components are unknown for these $\mathbf{k}$ directions. Calculation of the product $\tau\, \Delta\omega$ gives: 20, 9, and 4 for the three samples where, at least, the first two can be considered much larger than 1. Excitons of higher n reveal a much broader linewidth. We obtain for the 3S resonance a width of 290 μeV [Fig. 3(a)]. This corresponds to a lifetime of 4.6 ps and values of less than 0.1 for $\tau\, \Delta\omega$. Therefore, Eq. (32) is not fulfilled. An illustrative picture is that the three orthoexciton components of higher-n states are broader than the splitting by k^2 and strain terms. In consequence, they overlap in energy and cannot gain a relative phase between each other. It is important to note that we need to treat the 1S components as overlapping because the spectral resolution of the monochromator is not sufficient. Excitons of higher n cannot be resolved due to the fundamental restriction by their broader linewidths.

VII. CONCLUSIONS

We explain the unexpected observation of SHG along forbidden directions at the 1S exciton resonance of the yellow series in Cu_2O. Residual strain in the samples mixes and shifts the three states of the 1S orthoexciton. The mixing leads to new eigenstates that are two-photon dipole and one-photon quadrupole active at the same time, allowing for SHG. Furthermore, we find the energy splitting of the new SHG allowed eigenstates to be of importance. For a small splitting in energy, their interferences have to be considered. In contrast, for a large splitting each state can be regarded as independent.

The main achievement of this contribution is to introduce strain as a considerable factor, which allows one to describe qualitatively the characteristic polarization dependences for four different crystal orientations. Within a sample, the local strain depends strongly on the sample position as shown in Fig. 5. Despite the strain-free mounting of samples, residual strain might arise from sample preparation. By simulation of the rotational anisotropies shear strain components as small as 10^{-6} can be determined, corresponding to parts per 10^6 of the lattice constant only. This shows that the rotational SHG anisotropies are established as highly sensitive probes for strain-induced distortions. Moreover, the evaluation of the rotational diagrams gives insight into energy-level splittings on the μeV level which are hard to resolve in linear spectroscopy. Excitons of higher principal quantum number n, even though exposed also to strain, behave according to the expectation for point-group O_h. This is due to their shorter lifetimes and larger linewidths. Therefore, the splitting in energy is not large enough to separate the exciton components.

The connection between energy splitting and mixing of states is not restricted to local strain studied in this paper. It could be extended to a targeted external strain application to the sample to further prove our theoretical model and as a tool to tailor SHG as well as other perturbations, such as external magnetic and electric fields.

ACKNOWLEDGMENTS

We acknowledge the financial support by the Deutsche Forschungsgemeinschaft through the International Collaborative Research Centre TRR 160 (Project No. C8) and the Collaborative Research Centre TRR 142 (Project No. B01).

[1] Y. R. Shen, *The Principles of Nonlinear Optics* (Wiley, New York, 1984).

[2] R. W. Boyd, *Nonlinear Optics* (Academic-Elsevier, Burlington, 2008).

[3] D. Fröhlich, in *Aspects of Nonlinear Spectroscopy*, edited by J. Treusch, Festkörperprobleme, Advances in Solid State Physics Vol. 21 (Springer, Berlin/Heidelberg, 1981), p. 363.

[4] P. A. Franken, A. E. Hill, C. W. Peters, and G. Weinreich, Generation of Optical Harmonics, Phys. Rev. Lett. **7**, 118 (1961).

[5] J. J. Hopfield, J. M. Worlock, and Kwangjai Park, Two-Quantum Absorption Spectrum of KI, Phys. Rev. Lett. **11**, 414 (1963).

[6] H. Mahr, in *Two-Photon Absorption Spectroscopy*, edited by H. Rabin and C. L. Tang, Quantum Electronics Vol. 1A (Academic, New York, 1975), p. 285.

[7] D. Fröhlich, E. Mohler, and P. Wiesner, Observation of Exciton Polariton Dispersion in CuCl, Phys. Rev. Lett. **26**, 554 (1971).

[8] D. C. Haueisen and H. Mahr, Observation of the dispersion curve of CuCl with second harmonic generation, Phys. Lett. A **36**, 433 (1971).

[9] D. R. Yakovlev, V. V. Pavlov, A. V. Rodina, R. V. Pisarev, J. Mund, W. Warkentin, and M. Bayer, Exciton spectroscopy of semiconductors by the method of optical harmonics generation (review), Phys. Solid State **60**, 1471 (2018).

[10] E. F. Gross and N. A. Karryev, Doklady Academii Nauk USSR **84**, 261 (1952).

[11] T. Kazimierczuk, D. Fröhlich, S. Scheel, H. Stolz, and M. Bayer, Giant Rydberg excitons in the copper oxide Cu_2O, Nature (London) **514**, 343 (2014).

[12] M. Takahata and N. Naka, Photoluminescence properties of the entire excitonic series in Cu_2O, Phys. Rev. B **98**, 195205 (2018).

[13] M. Y. Shen, S. Koyama, M. Saito, T. Goto, and N. Kuroda, Second-harmonic generation resonant to the 1*S* orthoexciton level of cuprous oxide, Phys. Rev. B. **53**, 13477 (1996).

[14] J. Mund, D. Fröhlich, D. R. Yakovlev, and M. Bayer, High-resolution second harmonic generation spectroscopy with femtosecond laser pulses on excitons in Cu_2O, Phys. Rev. B. **98**, 085203 (2018).

[15] G. F. Koster, J. O. Dimmock, R. G. Wheeler, and H. Statz, *Properties of the Thirty-Two Point Groups* (M.I.T. Press, Cambridge, MA, 1963).

[16] D. Fröhlich, K. Reimann, and R. Wille, Time-resolved two-photon emission in Cu_2O, Europhys. Lett. **3**, 853 (1987).

[17] G. Dasbach, D. Fröhlich, H. Stolz, R. Klieber, D. Suter, and M. Bayer, Wave-Vector-Dependent Exciton Exchange Interaction, Phys. Rev. Lett. **91**, 107401 (2003).

[18] G. Dasbach, D. Fröhlich, R. Klieber, D. Suter, M. Bayer, and H. Stolz, Wave-vector-dependent exchange interaction and its relevance for the effective exciton mass in Cu_2O, Phys. Rev. B **70**, 045206 (2004).

[19] K. Yoshioka and M. Kuwata-Gonokami, Dark excitons in Cu_2O crystals for two-photon coherence storage in semiconductors, Phys. Rev. B **73**, 081202(R) (2006).

[20] R. G. Waters, F. H. Pollak, R. H. Bruce, and H. Z. Cummins, Effects of uniaxial stress on excitons in Cu_2O, Phys. Rev. B **21**, 1665 (1980).

[21] H.-R. Trebin, H. Z. Cummins, and J. L. Birman, Excitons in cuprous oxide under uniaxial stress, Phys. Rev. B **23**, 597 (1981).

[22] F. Schweiner, J. Main, G. Wunner, and C. Uihlein, Even exciton series in Cu_2O, Phys. Rev. B. **95**, 195201 (2017).

[23] F. Schweiner, J. Main, M. Feldmaier, G. Wunner, and Ch. Uihlein, Impact of the valence band structure of Cu_2O on excitonic spectra, Phys. Rev. B. **93**, 195203 (2016).

[24] J. I. Jang and J. P. Wolfe, Relaxation of stress-split orthoexcitons in Cu_2O, Phys. Rev. B. **73**, 075207 (2006).